



<b>Publication Year</b>	2020
<b>Acceptance in OA</b>	2025-03-20T10:26:07Z
<b>Title</b>	Far-ultraviolet aurora identified at comet 67P/Churyumov-Gerasimenko
<b>Authors</b>	Galand, M., Feldman, P. D., Bockelée-Morvan, D., Biver, N., Cheng, Y. -C., RINALDI, GIOVANNA, Rubin, M., Altwegg, K., Deca, J., Beth, A., Stephenson, P., Heritier, K. L., Henri, P., Parker, J. Wm., Carr, C., Eriksson, A. I., Burch, J.
<b>Publisher's version (DOI)</b>	10.1038/s41550-020-1171-7
<b>Handle</b>	<a href="http://hdl.handle.net/20.500.12386/36880">http://hdl.handle.net/20.500.12386/36880</a>
<b>Journal</b>	NATURE ASTRONOMY
<b>Volume</b>	4

# Far ultraviolet aurora identified at comet 67P/Churyumov-Gerasimenko

M. Galand<sup>1</sup>, P. D. Feldman<sup>2</sup>, D. Bockelée-Morvan<sup>3</sup>, N. Biver<sup>3</sup>, Y.-C. Cheng<sup>3</sup>, G. Rinaldi<sup>4</sup>, M. Rubin<sup>5</sup>,  
K. Altwegg<sup>5</sup>, J. Deca<sup>6,7</sup>, A. Beth<sup>1</sup>, P. Stephenson<sup>1</sup>, K. L. Heritier<sup>1</sup>, P. Henri<sup>8</sup>, J. Wm. Parker<sup>9</sup>,  
C. Carr<sup>1</sup>, A. I. Eriksson<sup>10</sup>, & J. Burch<sup>11</sup>

<sup>1</sup>*Department of Physics, Imperial College London, Prince Consort Road, London, SW7 2AZ, UK*

<sup>2</sup>*Department of Physics and Astronomy, The Johns Hopkins University, 3400 N. Charles Street,  
Baltimore, MD 21218, USA*

<sup>3</sup>*LESIA, Observatoire de Paris, Université PSL, CNRS, Sorbonne Université, Université de Paris,  
5 place Jules Janssen, 92195 Meudon, France*

<sup>4</sup>*IAPS-INAF, via del Fosso del Cavaliere, 100, 00133 Roma, Italy*

<sup>5</sup>*Physikalisches Institut, University of Bern, Sidlerstrasse 5, 3012 Bern, Switzerland*

<sup>6</sup>*Laboratory for Atmospheric and Space Physics (LASP), University of Colorado Boulder, Boulder,  
CO 80303, USA*

<sup>7</sup>*Institute for Modeling Plasma, Atmospheres and Cosmic Dust, NASA/SSERVI, Moffet Field, CA  
94035, USA*

<sup>8</sup>*LPC2E, CNRS, Université d'Orléans, 45071 Orléans, France*

<sup>9</sup>*Southwest Research Institute, Department of Space Studies, Suite 300, 1050 Walnut Street, Boul-  
der, CO 80302, USA*

<sup>10</sup>*Swedish Institute of Space Physics, Ångström Laboratory, Lägerhyddsvägen 1, 752 37 Uppsala,  
Sweden*

23 **Having a nucleus darker than charcoal, comets are usually detected from Earth through**  
24 **the emissions from their coma. The coma is an envelope of gas which forms through the sub-**  
25 **limation of ices from the nucleus, as the comet gets closer to the Sun. In the far ultraviolet,**  
26 **observations of comae have revealed the presence of atomic hydrogen and oxygen emissions.**  
27 **When observed over large spatial scales as seen from Earth, such emissions are dominated**  
28 **by resonance fluorescence pumped by solar radiation. Here we analyse data obtained close to**  
29 **the cometary nucleus by the Rosetta spacecraft. In order to identify their origin, we under-**  
30 **take a quantitative multi-instrument analysis of the far ultraviolet emissions by combining**  
31 **coincident neutral gas, electron, and spectroscopic observations together. We establish that**  
32 **the atomic emissions detected from Rosetta around comet 67P/Churyumov-Gerasimenko at**  
33 **large heliocentric distances result from the dissociative excitation of cometary molecules**  
34 **by accelerated solar-wind electrons (and not electrons produced from photo-ionisation of**  
35 **cometary molecules as suggested in past studies). We reveal their auroral nature. Similarly**  
36 **to the discrete aurorae at Earth and Mars, this newly-discovered cometary aurora is driven**  
37 **by the interaction of the solar wind with the local environment. We highlight how OI 1356 Å**  
38 **could be used as a tracer of solar-wind electron variability.**

39 The Rosetta spacecraft escorted comet 67P/Churyumov-Gerasimenko (referred as 67P here-  
40 after) for more than two years<sup>1,2</sup>. Onboard, the Alice ultraviolet imaging spectrograph<sup>3</sup> detected  
41 Far UltraViolet (FUV) atomic hydrogen and oxygen emissions<sup>4-7</sup> from the cometary coma. Spec-

42 troscopic analysis of these emissions shows that their origin seems to be consistent with the disso-  
43 ciative excitation of cometary molecules, such as H<sub>2</sub>O and O<sub>2</sub><sup>8</sup>, by electrons<sup>4,7</sup>. The same process  
44 is taking place at the Jovian moons, Ganymede<sup>9,10</sup> and Europa<sup>11</sup>, though the magnetic and particle  
45 environments are very different. Observed from Earth, the FUV atomic emissions from comets pri-  
46 marily result from the resonance fluorescence<sup>12</sup> pumped by solar radiation and occurring in atoms  
47 in the extended coma. These atoms are produced by photodissociation of cometary molecules by  
48 solar radiation. The electrons thought to be responsible for the excitation of FUV emissions ob-  
49 served from Rosetta are supposed to be photoelectrons resulting from the ionisation of cometary  
50 neutrals by solar Extreme UltraViolet (EUV) radiation<sup>4,7</sup>. This means that the FUV emissions  
51 are presumed to be dayglow which primarily results from the interaction of solar photons with an  
52 atmosphere or a coma. In contrast, auroral emissions – as defined here – originate from the interac-  
53 tion of energetic, extra-atmospheric particles with an atmosphere or, more generally, the envelope  
54 of gas surrounding a planetary body<sup>13</sup>. By “energetic”, we refer to particles energetic enough to  
55 trigger the excitation which leads to emission. The energy range varies with the auroral process.  
56 For dissociative excitation of water, the minimum energy required for the FUV lines analysed here  
57 are between 14 and 17 eV. The planetary body does not need to have an intrinsic magnetic field  
58 to host aurorae. However, to be auroral, emissions need to be driven by energetic particles whose  
59 source is external (that is, not locally produced, like photoelectrons).

60 Northern and southern lights, the so-called aurora illuminating the high latitude skies on  
61 Earth, have captured the human imagination for centuries. They are highly relevant for providing  
62 a snapshot of the particle energy input over the high latitude regions and play a key role in space

63 weather. Over the past half century, auroral emissions have been discovered at planets and moons  
64 in the Solar System<sup>13–15</sup> and beyond<sup>16</sup>. Aurora is a universal phenomenon, accessible to obser-  
65 vations and analysis: aurora is a tracer of plasma interaction, a remote-sensing of magnetic field  
66 configuration, and a fingerprint of particle sources and atmospheric species<sup>13</sup>. So far, at comets, au-  
67 roral emissions have been reported in the X-rays and EUV, resulting from the interaction of heavy  
68 solar-wind ions with cometary gases<sup>13,17</sup>. Here we undertake a multi-instrument analysis of FUV  
69 atomic emissions (HI Ly $\beta$  line and OI 1356 Å, and OI 1304 Å multiplets), by combining coincident  
70 Rosetta datasets together and comparing observed and modelled brightnesses. Observations of the  
71 energetic (10–200 eV) electron distribution, neutral gas (in situ and remote), and FUV emissions,  
72 acquired over similar time periods at large heliocentric distances ( $\geq 2$  AU), are linked together  
73 through a physics-based model (Fig. 1). We apply this approach to nadir- and limb-viewing con-  
74 figurations in order to underpin the mechanism producing the FUV atomic emissions, to identify  
75 the origin of the energetic source and to reveal the nature of the emissions.

76 In order to establish the source of the FUV atomic emissions in a quantitative manner, the  
77 multi-instrument analysis is applied to seven nadir-viewing cases (see Table 1). The selected cases  
78 correspond to viewing over the shadowed nucleus: this avoids any contamination of the FUV  
79 emissions by solar radiation reflected off the nucleus' surface<sup>6</sup>. We are only focusing on HI and  
80 OI emissions here: the selected cases are for viewing over the northern hemisphere where water is  
81 the dominant species in the coma during the periods of interest<sup>18,19</sup>.

82 Comparing observed (magenta) and modelled (black) FUV brightnesses for the five 2015–

83 2016 nadir-viewing cases shows that the HI and OI emissions are produced by the dissociative  
84 excitation of cometary neutrals by energetic electrons (Fig. 2). The composition ( $\text{H}_2\text{O}$ ,  $\text{CO}_2$ ,  $\text{CO}$ ,  
85 and  $\text{O}_2$ ) and total column density of the neutral gas are obtained from in situ observations from the  
86 Rosetta Orbiter Spectrometer for Ion and Neutral Analysis (ROSINA)<sup>20</sup>. The emission frequency is  
87 derived from differential electron flux measurements from the Rosetta Plasma Consortium (RPC)<sup>21</sup>  
88 (see Extended Data Fig. 1). The neutral and electron observations combined to compute the mod-  
89 elled FUV brightnesses were taken during the same time period as the FUV observations (see  
90 Methods). The last three cases (26 December 2015 at 08 UT and 17 April 2016 at 11 UT and  
91 22 UT) attest that in the absence of notable amounts of energetic electrons, as measured in situ  
92 by the RPC electron spectrometer (see Extended Data Fig. 1 and Extended Data Table 1), there  
93 are nearly no atomic FUV HI or OI emissions detected by the spectrograph (Fig. 2). This demon-  
94 strates that there are no other significant sources contributing to the FUV atomic emissions over  
95 the shadowed nucleus, beside dissociative excitation of cometary molecules by electrons. In par-  
96 ticular, photodissociative excitation of cometary molecules by solar photons do not seem to play  
97 any significant role here, as anticipated<sup>4</sup>.

98 The two 2014 cases (29 Nov at 18:00 UT, 10 Dec at 22:02 UT) correspond to a nadir pointing  
99 when Rosetta was located above the neck of the bi-lobed nucleus (Table 1). Comparing observed  
100 and modelled OI FUV brightnesses for these two cases, for which a pure water coma is assumed  
101 in the absence of in situ gas composition measurements, shows that the observed OI FUV bright-  
102 nesses are consistent with dissociative excitation of a nearly-pure water coma (Fig. 2-b). This  
103 confirms earlier findings that the coma over the neck is primarily composed of water<sup>4,18,19</sup>. In

104 this concave region, the outgassing is very active<sup>19</sup> and emanates in many directions, enhanced by  
105 self-illumination during low subsolar latitudes<sup>22</sup>. It is also difficult to derive the detailed activity of  
106 the surface in the neck. As a result, the water column density used as input to the model cannot be  
107 straightforwardly derived from the number density measured at Rosetta (combined with a simple  
108 extrapolation). It is instead set to give the modelled HI Ly $\beta$  brightness in agreement (within 4%)  
109 with the observed one (Fig. 2a and Table 1). The column density of  $(3.8 \pm 0.8) \times 10^{15} \text{ cm}^{-2}$ ,  
110 obtained for the 29 November 2014 case, is consistent with the value of  $(4.6 \pm 0.3) \times 10^{15} \text{ cm}^{-2}$   
111 derived from Visual InfraRed Thermal Spectrometer (VIRTIS)<sup>23</sup> observations (see Methods for  
112 details). The sensitivity of the OI modelled brightnesses by adding small amounts of O<sub>2</sub>, CO, or  
113 CO<sub>2</sub> to the assumed pure water coma is discussed in the Methods section.

114 In order to establish the origin of the energetic electrons responsible for the FUV auroral  
115 emissions, the multi-instrument analysis is applied to limb viewing (see Methods). In that con-  
116 figuration, the FUV spectrograph is staring off nadir at the cometary coma and observing FUV  
117 emissions produced in a region of the coma not located between the cometary nucleus and Rosetta.  
118 By linking FUV emissions from such a remote region with the emission frequency derived from  
119 in-situ electron flux measurements at Rosetta, we are assessing whether energetic electrons are ac-  
120 celerated/heated locally, or they have a large-scale external origin (e.g., hemispheric scale or more).  
121 In the former case, the FUV emissions should not be correlated with the energetic electrons, while  
122 in the latter, they should be. Without direct measurements of the detailed neutral composition in  
123 the remote region observed, the analysis is only applied to HI Ly $\beta$  which is solely driven by wa-  
124 ter. The modelled brightness is derived by multiplying the water column density deduced from

125 Microwave Instrument on the Rosetta Orbiter (MIRO)<sup>24</sup> measurements and VIRTIS infrared ob-  
126 servations (coincident with the FUV observation periods), with the HI Ly $\beta$  emission frequency  
127 derived from simultaneous in situ RPC electron flux measurements at Rosetta. Two limb-viewing  
128 intervals of two days in October 2014 have been analysed (Tables 1 and 2).

129 Past studies looked at the correlation between the limb brightness in HI Ly $\beta$  from Alice  
130 FUV spectrograph and the water column density from VIRTIS infrared spectrometer<sup>7</sup> and at the  
131 correlation between the limb brightness in OI 1356 Å from Alice and the energetic electron density  
132 from RPC<sup>25</sup>. In contrast, here the observed FUV brightness is quantitatively compared with the  
133 modelled brightness driven by simultaneous in situ observations of the energetic electron flux from  
134 RPC (taking into account the energy distribution of the electrons) and by the water column density  
135 measured remotely from Rosetta.

136 Comparing the HI Ly $\beta$  calculated (blue) and observed (magenta) brightnesses on 18–19 Oc-  
137 tober 2014 (Fig. 3-a) and 22–23 October 2014 (Fig. 3-b) confirms that overall the prime source of  
138 the HI Ly $\beta$  emissions is the dissociative excitation of water. There is a good agreement in terms of  
139 both magnitude and variability. The relative difference in magnitude is  $30\% \pm 21\%$  over all periods  
140 ( $13\% \pm 6\%$  for P3) on 18–19 October 2014; it is  $22\% \pm 18\%$  over all periods ( $11\% \pm 10\%$  for P3)  
141 on 22–23 October 2014. The contribution from resonance scattering driven by the interplanetary  
142 medium along the line of sight has been subtracted and amounts to  $\sim 1.5$  Rayleigh, while the con-  
143 tribution from the coma is negligible (see Methods). For a given time, the brightness averaged over  
144 the rows at the centre of the slit is shown with a dot, while the vertical, light pink bar extends from

145 the brightness from rows looking closest to the nucleus (upper bound) to the brightness from rows  
146 farthest away from the nucleus (lowest bound) for selected row ranges (see Table 1). The width of  
147 the pink bars corresponds to the FUV observation integration time (10 min). The observed limb  
148 brightnesses have a  $\pm 30\%$  uncertainty, shown with vertical, thin, magenta lines for three times on  
149 each panel.

150 The very good agreement between the observed and modelled brightnesses in Fig. 3 attests  
151 that the energetic electron fluxes measured at Rosetta are consistent with those driving the FUV  
152 emissions: the energetic electrons are not locally accelerated/heated. As the water column density  
153 is fixed over each FUV observation period  $Px$  (Table 2), the variations in the modelled brightness  
154 during  $Px$  is only driven by the variation in the RPC electron fluxes. The very good correlation  
155 between the observed and modelled brightness variations includes the overall decrease during P2  
156 on 18 October 2014, the sharp intensification at 16:30 UT and the drop at 21 UT on 22 October  
157 2014, and the decline over P4 on 23 October 2014. The sharp intensification at 16:30 UT, seen  
158 in both the modelled and the observed brightnesses, coincides with a large increase in the local  
159 plasma density and is associated with the arrival of a solar event<sup>26</sup>. The mean energy and number  
160 density of the energetic electrons increase suddenly, which yields an enhancement in both the  
161 emission and ionisation frequencies<sup>27</sup>.

162 Finally, though photoelectrons are present along the line of sight, they cannot constitute the  
163 bulk of the energetic electrons responsible for the FUV emissions. The source of the energetic pop-  
164 ulation must be external, as attested by the variability observed in the RPC electron differential flux

165 over the limb-viewing periods. Additional evidence is the anti-correlation between the electron-  
166 impact ionisation frequency and the local outgassing rate observed away from perihelion<sup>27,28</sup>.

167 The Rosetta multi-instrument analysis linking coincident particle, neutral gas, and FUV  
168 emission datasets together shows that the FUV emissions over the shadowed nucleus observed  
169 at large heliocentric distances are dominantly produced by the dissociative excitation of cometary  
170 molecules by energetic electrons. The auroral FUV OI emissions at Ganymede<sup>9,10</sup> and at Europa<sup>11</sup>  
171 are produced by the same type of excitation, while at Earth<sup>29</sup> and Venus<sup>30</sup> they are primarily in-  
172 duced by electron impact on atomic oxygen. However, the source of the energetic electrons is  
173 very different at comet 67P – subject to the interplanetary magnetic field frozen into the solar wind  
174 – compared with the ones at the Galilean moons, which are embedded in the intense magnetic  
175 field of Jupiter. The energetic electrons, found to be inducing the FUV emissions at comet 67P at  
176 large heliocentric distances, were already found to produce most of the ionisation in the coma<sup>27</sup>.  
177 They are hence responsible for the presence of a cometary plasma, denser (though colder) than the  
178 ambient solar wind, around the nucleus.

179 Applied to the limb viewing, the multi-instrument analysis demonstrates that the main source  
180 of the energetic electrons is not local (hence not photoelectrons as originally thought<sup>4,7</sup>). Based  
181 on the definition proposed for auroral emissions, this reveals the auroral nature of the FUV atomic  
182 emissions. We show that the source of energetic electrons involves a large-scale acceleration mech-  
183 anism. This finding is consistent with a particle-in-cell simulation applied to a weakly-outgassing  
184 comet<sup>31</sup> (Fig. 4). The self-consistent simulation shows that solar-wind electrons (red dots) undergo

185 acceleration primarily along the draped magnetic field lines when they fall into a potential well as  
186 they get closer to the cometary nucleus (trajectories color-coded by the electron energy in Fig. 4).  
187 This potential well is produced by an ambipolar electric field generated by the cometary plasma and  
188 resulting from the large electron pressure gradient<sup>31,32</sup>. This result confirms the original finding<sup>33</sup>  
189 that the observed energetic electron fluxes are too intense and energetic to be explained by un-  
190 perturbed photoelectrons or unperturbed solar-wind electrons, though they are consistent with the  
191 presence of an ambipolar electric field. At Earth, ambipolar electric fields (set up by electron pres-  
192 sure gradients between the cold, dense, ionospheric plasma and the hot, tenuous, magnetospheric  
193 plasma) are at least sometimes significant contributors to the large-scale, quasi-stationary, field-  
194 aligned electric fields observed in the auroral (upward field-aligned current) regions<sup>34</sup>. Similar to  
195 what is observed at comet 67P, these large-scale electric fields observed at Earth are responsible  
196 for the electron acceleration along the draped magnetic field lines. More generally, just like for  
197 discrete aurorae at Earth and Mars<sup>15,35</sup> (which result from the interaction of the terrestrial mag-  
198 netosphere and the martian remanent crustal magnetic field with the solar wind), we show that  
199 the energetic electrons at comet 67P are accelerated by large-scale electric fields arising from the  
200 interaction of the cometary plasma with the solar wind. Lacking an intrinsic magnetic field, the  
201 cometary aurora is diffuse, while the terrestrial and martian discrete aurorae are spatially confined.  
202 In contrast to the martian diffuse aurora<sup>36</sup>, it occurs even in the absence of solar energetic particle  
203 outbursts. While aurora is a universal process, the combination of the excitation process (the same  
204 as at Ganymede and Europa) and of the particle acceleration process (resulting from the interac-  
205 tion of the solar wind with the body through electric field acceleration, as for the discrete aurorae

206 at Earth and Mars) renders the FUV auroral emissions at comet 67P unique. The discovery of  
207 the presence of cometary auroral emissions induced by solar-wind electrons at large heliocentric  
208 distances offers the opportunity to use FUV emissions as a probe of the space environment at  
209 a comet location: observations of OI 1356 Å (emission not affected by resonance fluorescence)  
210 could be used as a proxy for solar-wind electron variability, which would be highly relevant for  
211 space weather applications.

## 212 **References**

- 213 1. Taylor, M. G. G. T., Altobelli, N., Buratti, B. J. & Choukroun, M. The Rosetta mission orbiter  
215 science overview: the comet phase. *Philos. Trans. R. Soc. A* **375**, 20160262 (2017).
- 216 2. Glassmeier, K.-H., Boehnhardt, H., Koschny, D., Kührt, E. & Richter, I. The Rosetta Mission:  
217 Flying Towards the Origin of the Solar System. *Space Sci. Rev.* **128**, 1–21 (2007).
- 218 3. Stern, S. A. *et al.* Alice: The Rosetta Ultraviolet Imaging Spectrograph. *Space Sci. Rev.* **128**,  
219 507–527 (2007).
- 220 4. Feldman, P. D. *et al.* Measurements of the near-nucleus coma of comet 67P/Churyumov-  
221 Gerasimenko with the Alice far-ultraviolet spectrograph on Rosetta. *Astron. Astrophys.* **583**,  
222 A8 (2015).
- 223 5. Feldman, P. D. *et al.* The Nature and Frequency of the Gas Outbursts in Comet  
224 67P/Churyumov-Gerasimenko Observed by the Alice Far-ultraviolet Spectrograph on Rosetta.  
225 *Astrophys. J. Lett.* **825**, L8 (2016).

- 226 6. Feldman, P. D. *et al.* FUV Spectral Signatures of Molecules and the Evolution of the Gaseous  
227 Coma of Comet 67P/Churyumov-Gerasimenko. *Astron. J.* **155**, 9 (2018).
- 228 7. Chaufray, J.-Y. *et al.* Rosetta Alice/VIRTIS observations of the water vapour UV electroglow  
229 emissions around comet 67P/Churyumov-Gerasimenko. *Mon. Not. R. Astron. Soc.* **469**, S416–  
230 S426 (2017).
- 231 8. Bieler, A. *et al.* Abundant molecular oxygen in the coma of comet 67P/Churyumov-  
232 Gerasimenko. *Nature* **526**, 678–681 (2015).
- 233 9. Feldman, P. D. *et al.* HST/STIS Ultraviolet Imaging of Polar Aurora on Ganymede. *Astrophys.*  
234 *J.* **535**, 1085–1090 (2000).
- 235 10. Molyneux, P. M. *et al.* Hubble Space Telescope Observations of Variations in Ganymede’s  
236 Oxygen Atmosphere and Aurora. *J. Geophys. Res. Space Phys.* **123**, 3777–3793 (2018).
- 237 11. Roth, L. *et al.* Transient Water Vapor at Europa’s South Pole. *Science* **343**, 171–174 (2014).
- 238 12. Lupu, R. E., Feldman, P. D., Weaver, H. A. & Tozzi, G.-P. The Fourth Positive System  
239 of Carbon Monoxide in the Hubble Space Telescope Spectra of Comets. *Astrophys. J.* **670**,  
240 1473–1484 (2007).
- 241 13. Galand, M. & Chakrabarti, S. Auroral Processes in the Solar System. *Washington DC Ameri-*  
242 *can Geophysical Union Geophysical Monograph Series* **130**, 55 (2002).
- 243 14. Drossart, P. *et al.* Detection of H<sub>3</sub><sup>+</sup> on Jupiter. *Nature* **340**, 539–541 (1989).
- 244 15. Bertaux, J.-L. *et al.* Discovery of an aurora on Mars. *Nature* **435**, 790–794 (2005).

- 245 16. Hallinan, G. *et al.* Magnetospherically driven optical and radio aurorae at the end of the stellar  
246 main sequence. *Nature* **523**, 568–571 (2015).
- 247 17. Lisse, C. M. *et al.* Discovery of X-ray and Extreme Ultraviolet Emission from Comet  
248 C/Hyakutake 1996 B2. *Science* **274**, 205–209 (1996).
- 249 18. Hässig, M. *et al.* Time variability and heterogeneity in the coma of 67P/Churyumov-  
250 Gerasimenko. *Science* **347**, aaa0276 (2015).
- 251 19. Migliorini, A. *et al.* Water and carbon dioxide distribution in the 67P/Churyumov-  
252 Gerasimenko coma from VIRTIS-M infrared observations. *Astron. Astrophys.* **589**, A45  
253 (2016).
- 254 20. Balsiger, H. *et al.* Rosina Rosetta Orbiter Spectrometer for Ion and Neutral Analysis.  
255 *Space Sci. Rev.* **128**, 745–801 (2007).
- 256 21. Carr, C. *et al.* RPC: The Rosetta Plasma Consortium. *Space Sci. Rev.* **128**, 629–647 (2007).
- 257 22. Keller, H. U. *et al.* Insolation, erosion, and morphology of comet 67P/Churyumov-  
258 Gerasimenko. *Astron. Astrophys.* **583**, A34 (2015).
- 259 23. Coradini, A. *et al.* VIRTIS: An Imaging Spectrometer for the Rosetta Mission. *Space Sci. Rev.*  
260 **128**, 529–559 (2007).
- 261 24. Gulikis, S. *et al.* MIRO: Microwave Instrument for Rosetta Orbiter. *Space Sci. Rev.* **128**,  
262 561–597 (2007).

- 263 25. Noonan, J. W. *et al.* Ultraviolet Observations of Coronal Mass Ejection Impact on Comet  
264 67P/Churyumov-Gerasimenko by Rosetta Alice. *Astron. J.* **156**, 16 (2018).
- 265 26. Witasse, O. *et al.* Interplanetary coronal mass ejection observed at STEREO-A, Mars, comet  
266 67P/Churyumov-Gerasimenko, Saturn, and New Horizons en route to Pluto: Comparison of  
267 its Forbush decreases at 1.4, 3.1, and 9.9 AU. *J. Geophys. Res. Space Phys.* **122**, 7865–7890  
268 (2017).
- 269 27. Heritier, K. L. *et al.* Plasma source and loss at comet 67P during the Rosetta mission. *Astron.*  
270 *Astrophys.* **618**, A77 (2018).
- 271 28. Galand, M. *et al.* Ionospheric plasma of comet 67P probed by Rosetta at 3 au from the Sun.  
272 *Mon. Not. R. Astron. Soc.* **462**, S331–S351 (2016).
- 273 29. Germany, G. A., Torr, M. R., Torr, D. G. & Richards, P. G. Use of FUV auroral emissions as  
274 diagnostic indicators. *J. Geophys. Res. Space Phys.* **99**, 383–388 (1994).
- 275 30. Fox, J. L. & Stewart, A. I. F. The Venus ultraviolet aurora - A soft electron source. *J. Geo-*  
276 *phys. Res.* **96**, 9821–9828 (1991).
- 277 31. Deca, J. *et al.* Building a weakly outgassing comet from a generalized ohm's law. *Phys. Rev.*  
278 *Lett.* **123**, 055101 (2019).
- 279 32. Divin, A. *et al.* A Fully Kinetic Perspective of Electron Acceleration around a Weakly Out-  
280 gassing Comet. *Astrophys. J. Lett.* **889**, L33 (2020).

- 281 33. Madanian, H. *et al.* Suprathermal electrons near the nucleus of comet 67P/Churyumov-  
282 Gerasimenko at 3 AU: Model comparisons with Rosetta data. *J. Geophys. Res. Space Phys.*  
283 **121**, 5815–5836 (2016).
- 284 34. Hull, A. J., Bonnell, J. W., Mozer, F. S., Scudder, J. D. & Chaston, C. C. Large parallel electric  
285 fields in the upward current region of the aurora: Evidence for ambipolar effects. *J. Geophys.*  
286 *Res. Space Phys.* **108**, 1265 (2003).
- 287 35. Lundin, R. *et al.* Plasma acceleration above martian magnetic anomalies. *Science* **311**, 980–  
288 983 (2006).
- 289 36. Schneider, N. M. *et al.* Discovery of diffuse aurora on Mars. *Science* **350**, 0313 (2015).
- 290 37. Burch, J. L. *et al.* RPC-IES: The Ion and Electron Sensor of the Rosetta Plasma Consortium.  
291 *Space Sci. Rev.* **128**, 697–712 (2007).
- 292 38. Makarov, O. P. *et al.* Kinetic energy distributions and line profile measurements of dissociation  
293 products of water upon electron impact. *J. Geophys. Res. Space Phys.* **109**, A09303 (2004).
- 294 39. Mumma, M. J., Stone, E. J., Borst, W. L. & Zipf, E. C. Dissociative Excitation of Vacuum Ul-  
295 traviolet Emission Features by Electron Impact on Molecular Gases. III. CO<sub>2</sub>. *J. Chem. Phys.*  
296 **57**, 68–75 (1972).
- 297 40. Ajello, J. M. Emission Cross Sections of CO by Electron Impact in the Interval 1260-5000 Å.  
298 I. *J. Chem. Phys.* **55**, 3158–3168 (1971).

- 299 41. Kanik, I. *et al.* Electron impact dissociative excitation of O<sub>2</sub>: 2. Absolute emission cross  
300 sections of the OI(130.4 nm) and OI(135.6 nm) lines. *J. Geophys. Res. Planets* **108**, 5126  
301 (2003).
- 302 42. Heritier, K. L. Cometary ionosphere analysis from Rosetta multi-instrument dataset. *PhD*  
303 *Thesis Imperial College London (UK)* (2018). <https://doi.org/10.25560/66101>.
- 304 43. Odelstad, E. *et al.* Measurements of the electrostatic potential of Rosetta at comet 67P. *Mon.*  
305 *Not. R. Astron. Soc.* **469**, S568–S581 (2017).
- 306 44. Eriksson, A. I. *et al.* RPC-LAP: The Rosetta Langmuir Probe Instrument. *Space Sci. Rev.* **128**,  
307 729–744 (2007).
- 308 45. Edberg, N. J. T. *et al.* Solar wind interaction with comet 67P: Impacts of corotating interaction  
309 regions. *J. Geophys. Res. Space Phys.* **121**, 949–965 (2016).
- 310 46. Le Roy, L. *et al.* Inventory of the volatiles on comet 67P/Churyumov-Gerasimenko from  
311 Rosetta/ROSINA. *Astron. Astrophys.* **583**, A1 (2015).
- 312 47. Gasc, S. *et al.* Sensitivity and fragmentation calibration of the time-of-flight mass spectrometer  
313 RTOF on board ESA's Rosetta mission. *Planet. Space Sci.* **135**, 64–73 (2017).
- 314 48. Jorda, L. *et al.* The global shape, density and rotation of Comet 67P/Churyumov-Gerasimenko  
315 from preperihelion Rosetta/OSIRIS observations. *Icarus* **277**, 257–278 (2016).

- 316 49. Bockelée-Morvan, D. *et al.* First observations of H<sub>2</sub>O and CO<sub>2</sub> vapor in comet  
317 67P/Churyumov-Gerasimenko made by VIRTIS onboard Rosetta. *Astron. Astrophys.* **583**,  
318 A6 (2015).
- 319 50. Dhiri, V. J. F., Vallat, C. & Kueppers, M. Rosetta: Payload boresight alignment details. *ESA*  
320 **2**, 1–11, doi: RO–EST–TN–3305 (2014).
- 321 51. Fougere, N. *et al.* Direct Simulation Monte Carlo modelling of the major species in the coma  
322 of comet 67P/Churyumov-Gerasimenko. *Mon. Not. R. Astron. Soc.* **462**, S156–S169 (2016).
- 323 52. Biver, N. *et al.* Long-term monitoring of the outgassing and composition of comet  
324 67P/Churyumov-Gerasimenko with the Rosetta/MIRO instrument. *Astron. Astrophys.* **630**,  
325 A19 (2019).
- 326 53. Fink, U. *et al.* Investigation into the disparate origin of CO<sub>2</sub> and H<sub>2</sub>O outgassing for Comet  
327 67P. *Icarus* **277**, 78–97 (2016).
- 328 54. Deca, J. *et al.* Electron and Ion Dynamics of the Solar Wind Interaction with a Weakly Out-  
329 gassing Comet. *Physical Review Letters* **118**, 205101 (2017).

330 **Acknowledgements** Rosetta is a European Space Agency (ESA) mission with contributions from its mem-  
331 ber states and the National Aeronautics and Space Administration (NASA). We acknowledge the continuous  
332 support of the Rosetta teams at the European Space Operations Centre in Darmstadt and at the European  
333 Space Astronomy Centre. We acknowledge the staff of CDDP and Imperial College for the use of AMDA  
334 and the RPC Quicklook database. This work has benefited from discussions within International Team 402:

335 Plasma Environment of Comet 67P after Rosetta at the International Space Science Institute (ISSI) (Bern,  
336 Switzerland). We acknowledge PRACE for awarding us access to Curie at GENCI@CEA, France. We  
337 warmly thank Nicolas Fougere for his help and advice using the ICES models. Work at Imperial College  
338 London was supported by STFC of UK under grant ST/N000692/1 and ST/P002250/1. The Alice team  
339 acknowledges support from NASA's Jet Propulsion Laboratory through contract 1336850 to the Southwest  
340 Research Institute. MR acknowledges the support of the State of Bern and the Swiss National Science  
341 Foundation (200021\_165869, 200020\_182418). J. D. gratefully acknowledges support from NASA's Rosetta  
342 Data Analysis Program, Grant No. 80NSSC19K1305, NASA's Solar System Exploration Research Virtual  
343 Institute (SSERVI): Institute for Modeling Plasmas, Atmosphere, and Cosmic Dust (IMPACT), and the com-  
344 putational resources provided by the NASA High-End Computing (HEC) Program through the NASA Ad-  
345 vanced Supercomputing (NAS) Division at Ames Research Center. We acknowledge PRACE for awarding  
346 us access to Curie at GENCI@CEA, France. Work at LPC2E/CNRS was supported by CNES and by ANR  
347 under the financial agreement ANR-15-CE31-0009-01. VIRTIS was built by a consortium, which includes  
348 Italy, France, and Germany, under the scientific responsibility of the Istituto di Astrofisica e Planetologia  
349 Spaziali of INAF, Italy, which also guides the scientific operations. The VIRTIS instrument development,  
350 led by the prime contractor Leonardo-Finmeccanica (Florence, Italy), has been funded and managed by ASI,  
351 with contributions from Observatoire de Meudon financed by CNES, and from DLR. We thank the Rosetta  
352 Science Ground Segment and the Rosetta Mission Operations Centre for their support throughout all the  
353 phases of the mission. The VIRTIS calibrated data will be available through the ESAs Planetary Science  
354 Archive (PSA) Website ([www.rssd.esa.int](http://www.rssd.esa.int)) and is available upon request until posted to the archive. We  
355 thank the following institutions and agencies for support of this work: Italian Space Agency (ASI, Italy)  
356 contract number I/024/12/1, Centre National d'Etudes Spatiales (CNES, France), DLR (Germany), NASA  
357 (USA) Rosetta Program, and Science and Technology Facilities Council (UK). All ROSINA data are the

358 work of the international ROSINA team (scientists, engineers and technicians from Switzerland, France,  
359 Germany, Belgium and the US) over the past 25 years, which we herewith gratefully acknowledge.

360 **Author contributions** M.G. led the study, performed the multi-instrument analysis, generated Fig. 2 and  
361 3, and wrote the manuscript. P.D.F. identified times of interest for Alice, analysed the FUV dataset, ad-  
362 vised on the different emission source mechanisms, and estimated the interplanetary medium contribution.  
363 D.B.-M. and Y.-C.C. analysed the VIRTIS-H dataset. N.B. analysed the MIRO dataset. G.R. analysed the  
364 VIRTIS-M dataset. M.R. and K.A. (Principal investigator of the ROSINA instrument) provided the ROSINA  
365 dataset. They all provided guidance on the interpretation of their respective dataset. J.D. generated Fig. 4  
366 based on the output of a PiC simulation he ran. J.D. and P.H. provided guidance on the PiC simulation  
367 interpretation. A.B., P.S. and K.L.H. provided feedback on the multi-instrument analysis. A.B. generated  
368 Fig. 1. J.Wm.P. (Principal investigator of the Alice instrument) contributed to the interpretation of the Alice  
369 dataset. C.C., A.I.E., and J.B. (all Principal investigators of RPC) provided guidance on the interpretation  
370 of the RPC dataset. A.I.E. provided the RPC-LAP dataset. All authors contributed to the interpretation of  
371 the results and commented on this manuscript.

372 **Interest declaration** The authors declare that they have no competing financial interests.

373 **Correspondence** Correspondence and requests for materials should be addressed to M. Galand (email:  
374 mgaland@ic.ac.uk).

## 375 **Methods**

376 We apply a multi-instrument analysis linking coincident Rosetta electron, neutral gas, and FUV emission  
377 observations together (Fig. 1). The measured FUV brightnesses for HI and OI emissions are compared with

378 the calculated brightnesses derived from electron and neutral gas measurements. The latter includes in situ  
379 measurements from a mass spectrometer as well as remote-sensing sub-mm and infrared observations. The  
380 auroral nature that we derive for the FUV emissions is consistent with a particle-in-cell simulation applied  
381 to low outgassing comets.

382 **Modelled FUV brightnesses.** We calculate the brightness of three atomic emissions, HI Ly $\beta$  line (1026 Å)  
383 and OI multiplets (1304 Å and 1356 Å), for seven cases in nadir viewing over the shadowed nucleus and for  
384 two periods of two days in limb viewing (Table 1). The number of cases is restricted by the requirements  
385 (1) to have analysed FUV brightness observations, with high enough signal to noise, over the northern  
386 hemisphere, (2) for the nadir study, to have the FUV spectrograph viewing along the nadir over the shadowed  
387 nucleus and to have simultaneous in situ neutral density and composition measurements (though two cases  
388 without neutral composition were included as they were over the nucleus' neck where the coma is known  
389 to be almost pure water), (3) for the limb study, to have coincident limb-viewing observations from the  
390 FUV spectrograph and from either the sub-mm instrument or one of the infrared sensors. The brightness  
391 (in Rayleigh) of an atomic emission  $X$  is assumed to be produced by the dissociative excitation of neutral  
392 molecules by energetic electrons. It is assessed, as a function of the time  $t$ , as follows:

$$B^X(t) = 10^{-6} \nu^X(t) C(t) \quad (1)$$

393 where  $\nu^X$  is the combined frequency (in s $^{-1}$ ) of dissociative excitation of neutral cometary species which  
394 contribute to the production of the atomic emission  $X$  and  $C$  is the total column density (in cm $^{-2}$ ), along the  
395 line of sight, of these neutral species. As HI Ly $\beta$  is only produced by the dissociation of water, its brightness  
396 is derived from the emission frequency of water and the water column density along the line of sight. As  
397 the OI emissions are induced by the dissociation of several neutral species, their brightnesses are calculated  
398 from the combined emission frequency (defined hereafter) and the total column density of H $_2$ O, CO $_2$ , CO,

399 and O<sub>2</sub> along the line of sight. For the nadir viewing, the modelled value provided for each case derives  
 400 from the average value over all measurements of RPC–Ion and Electron Sensor (IES)<sup>37</sup> over the observing  
 401 time of Alice (Fig. 2 and Table 1). For the limb viewing, the modelled values are provided at each time that  
 402 an energetic electron spectrum of RPC–IES is measured (Fig. 3). The typical time resolution of RPC–IES  
 403 over the selected limb-viewing days is 4 min.

404 *Electron-impact emission frequency:* The emission frequency  $\nu_n^X$  of the atomic emission  $X$  (HI Ly $\beta$ ,  
 405 OI 1304, OI 1356) associated with the dissociation of the neutral species  $n$  (H<sub>2</sub>O, O<sub>2</sub>, CO<sub>2</sub>, CO) is cal-  
 406 culated at time  $t$  at the location of Rosetta as follows:

$$\nu_n^X(t) = \int_{E_n^X}^{E_{max}} \sigma_n^X(E) J_e(t, E) dE \quad (2)$$

407 where  $\sigma_n^X(E)$  is the dissociative excitation cross section (in cm<sup>2</sup>) of  $n$  by an electron of energy  $E$  and  
 408  $J_e(t, E)$  is the differential electron flux (in cm<sup>-2</sup> s<sup>-1</sup> eV<sup>-1</sup>) measured at time  $t$ . We consider cross sections  
 409 from H<sub>2</sub>O yielding HI Ly $\beta$  and OI emissions<sup>38</sup>, from CO<sub>2</sub> yielding OI 1304<sup>39</sup> and OI 1356<sup>4</sup>, from CO  
 410 yielding OI multiplets<sup>40</sup>, and from O<sub>2</sub> yielding OI multiplets<sup>41</sup>.  $J_e$  can be assumed to be constant along  
 411 the line of sight<sup>7,27</sup>. It is obtained from the electron intensity (in cm<sup>-2</sup> s<sup>-1</sup> eV<sup>-1</sup> sr<sup>-1</sup>) measured by the  
 412 RPC–IES, after integrating the latter over elevation and azimuthal angles and assuming isotropy for blind  
 413 spots due to obstruction or the limited field of view<sup>42</sup>. The differential electron flux is also corrected for the  
 414 spacecraft potential<sup>43</sup> – obtained from RPC–LAP<sup>44</sup> – by applying Liouville’s theorem<sup>28</sup>. On 10 December  
 415 2014, as no data is available for the spacecraft potential  $V_{sc}$ , it was set to  $-10$  V. The arrival of a CIR on  
 416 22 October 2014 at 16:30 UT rendered the spacecraft potential very negative but could not be derived from  
 417 RPC–LAP over the rest of the day and the next day until 06 UT<sup>45</sup>. From 16:30 UT onward on 22 October  
 418 2014  $V_{sc}$  is set to  $-25$  V (part of P1 and period P2), while on 23 October 2014 which was less disturbed, it is  
 419 set to  $-15$  V (periods P3 and P4). The RPC–IES dataset is not reliable after 17:25 UT on 22 October 2014

420 for about 15-20 min, so it is disregarded. The energy  $E_{max}$  is the maximum energy considered which is set  
 421 to 200 eV; beyond this value, the signal is primarily at the background level. We check that the emission  
 422 frequency is not sensitive to the choice of a higher value for  $E_{max}$ , testing it up to 400 eV. The energy  $E_n^X$   
 423 represents the energy threshold of the dissociative excitation process; its value is 17 eV for HI Ly $\beta$  from  
 424 the dissociation of H<sub>2</sub>O; it varies between 14-15 eV (H<sub>2</sub>, O<sub>2</sub>) to 20-21 eV (CO, CO<sub>2</sub>) for the OI emissions.  
 425 When  $V_{sc}$  is very negative, the corrected differential electron flux from RPC–IES starts at an energy  $E_{min}$   
 426 above the ionisation threshold. In that case, it is extrapolated towards lower energies assuming a constant  
 427 value equal to the measured value at  $E_{min}$ . Figure ?? shows two examples of differential electron fluxes, as  
 428 a function of energy, measured by the RPC–IES electron spectrometer and used in the nadir study: one taken  
 429 at 11:47 UT (orange crosses) during the FUV observation period on 29 March 2015 starting at 11:43 UT  
 430 and the other taken at 08:35 UT (red pluses) taken during the FUV observation period on 26 December  
 431 2015 (Table 1). The differential fluxes are corrected for the spacecraft potential; as, by coincidence, the  
 432 latter is of the same order in both cases ( $-2$  V), the spectra start at about the same energy (about 8.5 eV).  
 433 By integration, the density of electrons with energies between 10 eV and 200 eV is derived and found to be  
 434 30 times higher in the March case than in the December case. The former is associated with a period when  
 435 significant FUV emissions are detected, while the latter is associated with a period of absence of significant  
 436 FUV emissions (see Figure 2).

437 Unlike HI Ly $\beta$  which is only induced by the dissociation of water, OI emissions are produced by the dis-  
 438 sociative excitation of all four major species. In that case, it is necessary to assess an effective emission  
 439 frequency, defined as:

$$\nu^X(t) = \sum_n v_n(t) \nu_n^X(t) \quad (3)$$

440 where  $v_n(t)$  is the volume mixing ratio of the neutral species  $n$  at time  $t$ . It is derived from the analysis

441 of the ROSINA–DFMS dataset obtained during the observing period of Alice. The data processing and  
 442 analysis of ROSINA-DFMS to derive the neutral composition are described in Le Roy et al.<sup>46</sup>. The neutral  
 443 composition is assumed to be constant in the nadir-viewing column of the coma. When it is not available  
 444 (e.g., 2014 nadir-viewing cases), the forward modelling is performed for a pure-water coma. The closest  
 445 DFMS measurements to one of the 2014 nadir-viewing cases was made on 10 December 2014 at 22 UT.  
 446 It shows that, after water, O<sub>2</sub> was the second most abundant species (3%), followed by CO (2%) and CO<sub>2</sub>  
 447 (0.7%) with a decreasing trend (with respect to water) observed from 20 UT to 22 UT. This trend suggests  
 448 that the mixing ratios of the minor species during the Alice observation window (22:02–23:13 UT) are likely  
 449 to be smaller than those listed above. The modelled OI brightnesses for pure water are shown in Fig. 2b.  
 450 For the 10 December 2014 case, while the OI 1304 brightnesses agree within the uncertainty, the OI 1356  
 451 brightness is ~45% lower compared with the Alice brightness (which has an absolute calibration uncertainty  
 452 of ±20%). Adding 0.5% of O<sub>2</sub> (relative to water) brings the modelled OI brightness within 5% of the  
 453 Alice OI 1356 brightness (electron impact on O<sub>2</sub> being efficient to produce OI 1356<sup>41</sup>), without affecting  
 454 significantly the OI 1304 modelled brightness (which remains within ~15% of the observed brightness), as  
 455 OI 1304 is dominantly produced through the dissociation of water<sup>38</sup>. Adding 2% of CO (or 1% of CO<sub>2</sub>) to  
 456 the H<sub>2</sub>O–O<sub>2</sub> coma, the OI 1356 modelled brightness is higher compared with the Alice brightness by 3–9%  
 457 (12–16%), respectively, but remains within the uncertainties of the observed value.

458 *Nadir column density:* For nadir viewing, the total neutral column density along the line of sight corresponds  
 459 to the number of molecules per unit area in the column between the Rosetta spacecraft and the surface of  
 460 the nucleus. By default, the column density is derived from the total neutral density  $n_{tot}^{COPS}(t, r)$  measured  
 461 at time  $t$  at the Rosetta cometocentric distance  $r_R$ , by the ROSINA–Comet Pressure Sensor (COPS)<sup>20</sup>,  
 462 after correction<sup>47</sup> for neutral composition inferred from ROSINA–DFMS. We assume a  $r^{-2}$ -dependence in

463 cometocentric distance  $r$  for the number density down to the surface, as justified by observations<sup>8,18</sup>. This  
 464 means that for nadir viewing, the column density at time  $t$  is:

$$C^{\text{COPS}}(t) = n_{\text{tot}}^{\text{COPS}}(t, r_R) \frac{(r_R - r_S) r_R}{r_S} \quad (4)$$

465 where  $r_S$  is the cometocentric distance of the nucleus' surface, assumed here to be a mean value of 1.7 km<sup>48</sup>.  
 466 Values derived for the column density are given in Table 1 for the four 2015–2016 nadir cases and in Table 3  
 467 for the two times selected in Fig. ??.

468 For the two 2014 nadir cases, which correspond to cases above the highly active neck of the bi-lobed  
 469 nucleus<sup>48</sup>, the geometry of the surface means that the gas is emitted in many directions with enhanced level  
 470 due to self-illumination<sup>22</sup>. It is not realistic to infer the column density close to the nucleus from measure-  
 471 ments of the neutral density at Rosetta. Instead, the water column density is derived from the comparison  
 472 between the observed and modelled HI Ly $\beta$  brightnesses (Table 1).

473 *Nadir column density on 29 November 2014:* Based on the HI Ly $\beta$  analysis, we derive a value of  $(3.8 \pm$   
 474  $0.8) \times 10^{15} \text{ cm}^{-2}$  (uncertainty linked to the 20% uncertainty in the observed nadir HI Ly $\beta$  brightness) for the  
 475 water column density for the 29 November 2014 case and used it to drive the model. This value is consistent  
 476 with the water column density value of  $(4.6 \pm 0.3) \times 10^{15} \text{ cm}^{-2}$  obtained from the high spectral-resolution  
 477 single-aperture spectrograph, VIRTIS–H<sup>49</sup> (H for High resolution) during the Alice observation period on  
 478 the same day. It should be noted that there may be a slight difference in the close-up regions seen by Alice  
 479 and VIRTIS–H at such a small distance from the nucleus, as highlighted by comparing their boresights and  
 480 fields of view<sup>50</sup>: Alice brightness is from bins 15–17 along the slit (Table 1), while VIRTIS–H aperture is  
 481 closest to the bin 14/15 junction; the field of view of VIRTIS–H ( $0.03^\circ \times 0.1^\circ$ )<sup>49</sup> is slightly smaller than  
 482 that associated with a bin of Alice ( $0.05^\circ \times 0.3^\circ$ )<sup>6</sup>. There is also a slight difference in the time period of  
 483 the two observation sets: 17:57–18:22 UT (VIRTIS–H), 18:00–18:40 UT (Alice). The derived value for

484 the water column density is also close to the value of  $6 \times 10^{15} \text{ cm}^{-2}$  deduced from the DSMC model for  
485 the region of interest<sup>51</sup>. As expected over the neck region, the water column density extrapolated from the  
486 neutral density measurements at Rosetta from ROSINA and assuming a mean cometocentric distance of the  
487 nucleus' surface of 1.7 km<sup>48</sup> is significantly smaller than the one deduced from VIRTIS-H (by 84%) and  
488 the one derived from HI Ly $\beta$  (82%).

489 *Limb column density:* For limb viewing, the column to consider along the viewing direction stretches from  
490 the Rosetta spacecraft to infinity. In practice, it extends up to where the coma is dense enough to emit  
491 significant emissions to be detected by the remote-sensing instruments. Only HI Ly $\beta$ , induced by the disso-  
492 ciation of water, is analysed for limb cases. The water column density is derived from the Rosetta sub-mm  
493 MIRO instrument and from the IR VIRTIS instrument suite. Microwave emissions at wavelengths near  
494 0.53 mm emitted by H<sub>2</sub><sup>18</sup>O and observed by the high-resolution spectrograph from MIRO<sup>24</sup> were analysed  
495 in order to derive the water column density<sup>52</sup>. An expansion velocity of 0.68 km s<sup>-1</sup> was assumed for the  
496 analysis of the limb observations. The  $\nu_3$  vibrational band of water near 2.7  $\mu\text{m}$ , the strongest vibrational  
497 band observed in cometary infrared spectra, was detected by VIRTIS<sup>23</sup>. Emission intensities from the high  
498 spectral-resolution single-aperture spectrograph, VIRTIS-H, were analysed in the 2.61–2.73  $\mu\text{m}$  range in  
499 order to derive water column density. The data processing and analysis of such a dataset are described in  
500 Bockelée-Morvan et al.<sup>49</sup>. Emission intensities from the infrared channel of the medium-resolution imaging  
501 spectrometer, VIRTIS-M (M for Mapper), were analysed by integrating over the 2.6–2.8  $\mu\text{m}$  band after  
502 subtracting the background continuum<sup>19,53</sup>.

503 The water column density values used for calculating the FUV HI Ly $\beta$  brightnesses during each limb-  
504 viewing period are listed in the fourth column in Table 2 along with the values observed by the MIRO in-  
505 strument in the sub-mm (fifth column), by the VIRTIS IR high-resolution spectrograph (sixth column) and

506 medium-resolution imaging spectrometer (seventh column). For period P3 of Alice observations (around  
507 midnight on 18 October 2014), measurements from all three remote sensors are available and agree very  
508 well. For the other periods, when available the water column densities derived from the IR medium-  
509 resolution imaging spectrometer are consistent with those derived from the sub-mm observations. As the  
510 water column density derived from the sub-mm instrument has the lowest uncertainty, we set the value used  
511 for the limb-viewing calculation to its mean value.

512 **Observed FUV brightnesses.** The FUV brightnesses are derived from the Alice imaging spectrograph<sup>3</sup> for  
513 nadir and limb-staring viewings. Among HI lines,  $\text{Ly}\beta$  is preferable to the stronger  $\text{Ly}\alpha$  for the present study  
514 due to the complexity of instrumental effects for Alice measurements. For limb viewing, the signal is also  
515 affected by the resonance scattering of the interplanetary H Lyman series, which is at least 300 times brighter  
516 in HI  $\text{Ly}\alpha$  than in HI  $\text{Ly}\beta$ . Even for nadir viewing over the shadowed nucleus, where such a contribution  
517 is not significant, the  $\text{Ly}\alpha$  sensitivity varies by a factor of 2 along the slit due to the uneven photocathode  
518 deposited on the microchannel plate detector in the region of  $\text{Ly}\alpha$ <sup>3</sup>.

519 For each bin along the slit, an individual spectrum is obtained after a time integration of typically 10 min.  
520 The slit has a dog-bone shape with a narrow, central region of width  $0.05^\circ$  and of length  $2^\circ$ <sup>3</sup>, spanning from  
521 bins 12 to 18 ( $0.3^\circ/\text{bin}$ ). The brightnesses for nadir viewing and the main brightnesses for limb viewing  
522 (magenta dots in Figure 3) are obtained from the central part of the narrow region of the slit, which provides  
523 the best spectral resolution possible with Alice. The central bin of the narrow region of the slit, bin 15,  
524 represents the closest bin to nadir when the  $z$  axis is nadir. All nadir viewing brightnesses are associated  
525 with a bin range including bin 15 (see Table 1). The only exception is 26 December 2015 which is slightly  
526 off nadir and, to a lesser extent, 17 April 2016. For limb viewing, beside the brightness around the slit's  
527 centre, two other brightnesses are given at each time, one generated from bins closer to the nucleus and

528 another one from bins further away from the nucleus (Table 1).

529 Once the spectra are co-added over the bin range and the count rate converted into a value in photons $\cdot$ R $^{-1}$ ,  
530 the spectra are sometimes averaged over time in order to improve the signal-to-noise ratio. This is done for  
531 the nadir observations over the shadowed nucleus. This explains why the observing periods, which are the  
532 sum of individual exposures, are ranging from 20 min to over 1 h 30 min (Table 1). For the limb viewing,  
533 the original 10-min integration has been conserved. After removal of the background derived from spectral  
534 regions cleared of strong lines, the brightness is estimated from integration over the atomic emission.

535 The HI and OI brightnesses for two nadir-viewing cases (29 November 2014 at 18:00 UT and 29 March 2015  
536 at 11:43 UT) have already been published<sup>6</sup> and further information on the Alice data analysis can be found  
537 there. The HI Ly $\beta$  brightnesses for the two limb-viewing cases (18–19 October 2014 and 22–23 October  
538 2014) are updated from Figs. 4 and 5 of Feldman et al.<sup>4</sup>, as since the publication the instrument calibration  
539 has been revised. The contribution of resonance scattering from the coma and the interplanetary medium  
540 (IPM) is estimated along the line of sight for these two observation periods. The contribution from the coma  
541 is assessed to be of the order of mR assuming a spherically symmetric neutral coma: it can be reliably  
542 neglected. The contribution from interplanetary HI is estimated based on nearly concurrent measurements  
543 made at larger off-nadir angles (and during a period of low measured electron flux). The uncertainty on the  
544 Alice limb brightnesses, including calibration uncertainty and IPM contribution, is estimated to be  $\pm 30\%$ .

545 **Particle-in-cell simulations.** To illustrate the large-scale energisation of electrons, we present the results  
546 of a 3D fully kinetic particle-in-cell simulation applied to a weakly-outgassing comet at large heliocentric  
547 distances<sup>54</sup>. The plasma environment is simulated for an heliocentric distance of 4 AU and an outgassing  
548 rate for the cometary nucleus of  $10^{25}$  s $^{-1}$ <sup>31</sup>. The simulation shows that the solar-wind electrons, originally  
549 at  $\sim 10$  eV, are accelerated towards the nucleus as they fall into the potential well produced by an ambipolar

550 electric field. This electric field is set up by the cometary plasma and is triggered by a strong electron  
551 pressure gradient (Fig. 4).

552 **Data Availability:** The Rosetta data that support the plots within this paper and other findings of this study  
553 are available from the ESA–PSA archive (<https://www.cosmos.esa.int/web/psa/rosetta>) or the NASA PDS  
554 archive ([https://pdssbn.astro.umd.edu/data\\_sb/missions/rosetta/index.shtml](https://pdssbn.astro.umd.edu/data_sb/missions/rosetta/index.shtml))

555 **Code Availability:** iPIC3D is publicly available on GitHub (<https://github.com/iPIC3D/iPIC3D>; Apache  
556 License 2.0).

Figure 1: **Multi-instrument approach applied to analyse FUV atomic emissions.** Overview of the generation of auroral emissions through the dissociative excitation of cometary molecules by energetic (10–200 eV) electrons. A multi-instrument approach is applied to confirm the origin of the FUV emissions by linking (a) the energetic electrons measured in situ by the Rosetta Plasma Consortium (RPC)<sup>21</sup> electron spectrometer<sup>37</sup>, (b) the cometary molecules observed in situ by the Rosetta Orbiter Spectrometer for Ion and Neutral Analysis (ROSINA)<sup>20</sup> and remotely by the Microwave Instrument on the Rosetta Orbiter (MIRO)<sup>24</sup>, and the Visual InfraRed Thermal Spectrometer (VIRTIS)<sup>23</sup>, and (c) the FUV atomic emissions detected by the Alice FUV spectrograph<sup>3</sup>.

Figure 2: **Nadir-viewing analysed cases.** Nadir-viewing FUV brightnesses observed (magenta) and calculated (black) from a combination of coincident neutral gas and electron measurements (a) for HI Ly $\beta$  line and (b) for OI 1304 Å (filled circles) and OI 1356 Å (filled triangles) multiplets. The magenta vertical bars include 20% uncertainty in the observed brightness values and  $\pm 1\sigma$  standard deviation resulting from the spread over the spatial rows in the extracted spectrum. The black vertical bars represent the variability in Rosetta in situ electron fluxes over the FUV observing time combined, for the OI brightnesses, with 20% in Rosetta in situ neutral composition uncertainty (except for the 2014 cases for which a pure water coma is assumed over the neck in the absence of coincident neutral composition observations). Measured and modelled points are offset for a given time for visibility.

Figure 3: **Limb-viewing analysed cases.** Time series of limb-viewing observed (magenta) and calculated (blue) HI Ly $\beta$  brightnesses (a) on 18–19 October 2014 and (b) on 22–23 October 2014. The model is driven by Rosetta in situ electron measurements and by the water column density derived from Rosetta remote-sensing sub-mm and IR observations (see Table 2). The observed FUV brightness is averaged over the rows at the centre of the slit (dot) and its uncertainty is  $\pm 30\%$  (vertical, thin, magenta lines for three times on each panel). The vertical, light pink bar shows the variation along the slit; its width corresponds to the FUV spectrograph integration time (10 min).

Figure 4: **Source of the energetic electrons.** Trajectories of solar-wind electrons inducing the FUV aurora around comet 67P. They undergo acceleration through the ambipolar electric field set up by the cometary plasma. The electron trajectories are shown with lines colour-coded by energy and the ambipolar electric field acting on electrons ( $-\mathbf{E}_{ambi}$ ), with green arrows. They are output from a 3D fully kinetic particle-in-cell simulation applied to a weakly-outgassing comet<sup>31</sup>. The upstream solar wind flows along +X (towards the right), the upstream interplanetary magnetic field points along +Y (upward), and Z is complementing the orthogonal coordinate system (out of the plane). The nucleus is not to scale.

Figure 5: **Extended Data Fig.1. Examples of differential electron fluxes measured by the RPC–IES electron spectrometer.** The fluxes were observed at 11:47 UT on 29 March 2015 (orange crosses) and at 08:35 UT on 26 December 2015 (red pluses) during two nadir-viewing FUV observation periods. The fluxes are corrected for the spacecraft potential<sup>28</sup> ( $-2$  V). By integration, the number density and mean energy of electrons with energies between 10 eV and 200 eV are derived and given in Extended Data Table 1.

**Table 1: Details on the analysed cases.** For nadir viewing, are given: selected day, Alice FUV spectrograph observation start time  $t_0$  and duration  $\Delta t$  (sum of all integration times used), bin number range used along the FUV spectrograph slit, heliocentric distance  $r_h$ , Rosetta cometocentric distance  $r_R$  and sub-spacecraft latitude at  $t_0$ , and column density  $C$  between Rosetta and the nucleus' surface. For limb viewing, are given: selected day, range of bins along the FUV spectrograph slit from closest to the nucleus, centre of the slit, to furthest from the nucleus, distances  $r_h$  and  $r_R$ , FUV spectrograph off-nadir viewing angle, and integration time  $\Delta t$ .

Nadir viewing against the shadowed nucleus							
Selected day	$t_0$	$\Delta t$	Bin #	$r_h$	$r_R$	Lat.	$C$
	(UT)	(hh:mm)	range <sup>a</sup>	(AU)	(km)	(°)	(10 <sup>15</sup> cm <sup>-2</sup> )
29 Nov 2014	18:00:01	00:40	15–17	2.87	30	51	3.8 <sup>b</sup>
10 Dec 2014	22:02:29	01:11	13–16	2.80	20	36	3.5 <sup>b</sup>
29 Mar 2015	01:04:00	00:20	13–14	1.99	43.1	14	3.5±0.1 <sup>c</sup>
29 Mar 2015	11:43:43	00:20	14–15	1.99	92	7	7.0±1.1 <sup>c</sup>
26 Dec 2015	08:05:16	01:11	09–12	1.98	79	28	4.5±0.5 <sup>c</sup>
17 Apr 2016	11:11:00	01:37	12–14	2.82	63	80	0.23±0.02 <sup>c</sup>
17 Apr 2016	22:28:00	01:17	12–14	2.82	54	82	0.26±0.02 <sup>c</sup>
Limb viewing							
Selected days	Bin #	Bin #	Bin #	$r_h$	$r_R$	off nadir	$\Delta t$
	closest	centre	furthest	(AU)	(km)	(°)	(min)
18-19 Oct 2014	8–12	13–17	18–22	3.16–3.15	10	15	10
22-23 Oct 2014	8–12	13–17	18–22	3.13–3.12	10	17	10

<sup>a</sup> The centre of the slit, closest to nadir, is bin 15. <sup>b</sup> The total column density is deduced from HI Ly $\beta$  observations

assuming a water pure coma (see text). <sup>c</sup> The total column density is derived from the total number density  $n_{tot}^{COPS}$  measured by the ROSINA-COPS pressure gauge, assuming a mean cometocentric distance for the nucleus' surface of 1.7 km<sup>48</sup> and the neutral composition derived from the ROSINA-DFMS mass spectrometer.

Table 2: **Water column density for the limb cases.** Are given the period  $Px$  selected, the date, the time range of  $Px$  (corresponding to the sub-mm observing period), the value  $C^{limb}$  of the water column density used for the calculation of the FUV brightness (see Figure 3), based on the measurements of the column density by the MIRO instrument in the sub-mm ( $C^{MIRO}$ ), by the IR high-resolution spectrograph ( $C^{VIRTIS-H}$ ) and by the medium-resolution imaging spectrometer ( $C^{VIRTIS-M}$ ). When no data is available, the column density entry is left blank. The remote-sensing IR measurements are made over approximately the same time range as the sub-mm observations (third column), though there are sometimes some departures in terms of the start or end times (up to 15 min) between instruments.

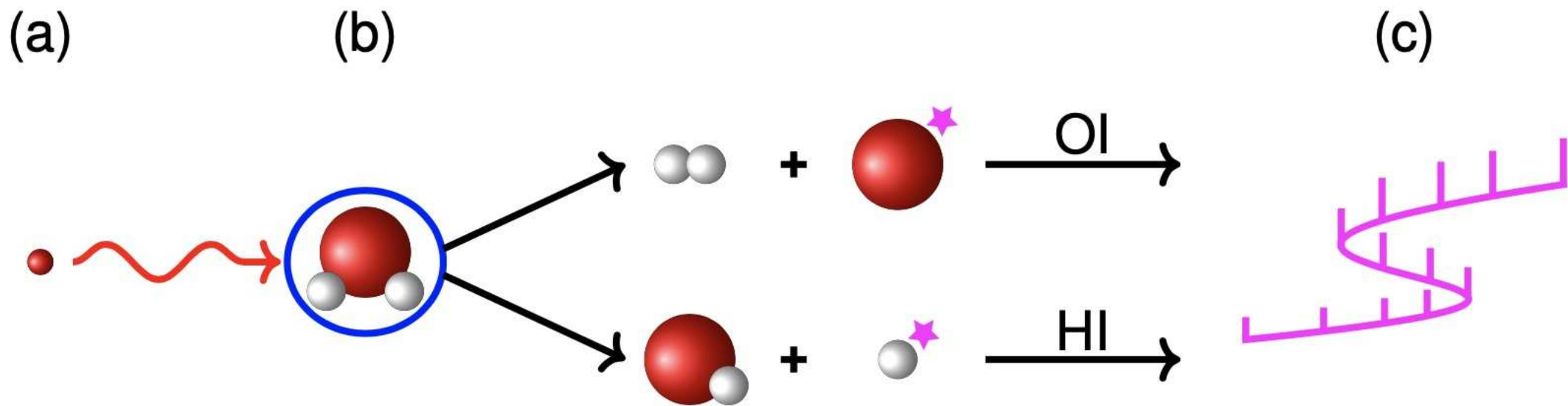
18-19 December 2014						
Selected period	Day	Time range (UT)	$C^{limb}$ ( $10^{15} \text{ cm}^{-2}$ )	$C^{MIRO}$ ( $10^{15} \text{ cm}^{-2}$ )	$C^{VIRTIS-H}$ ( $10^{15} \text{ cm}^{-2}$ )	$C^{VIRTIS-M}$ ( $10^{15} \text{ cm}^{-2}$ )
P1	18 Dec 2014	15:30 – 17:40	1.4	$1.41 \pm 0.07$		$1.6 \pm 0.7$
P2	18 Dec 2014	18:45 – 21:40	2.0	$2.04 \pm 0.07$		$2.1 \pm 0.9$
P3	18–19 Dec 2014	23:40 – 01:40	2.9	$2.87 \pm 0.09$	$2.8 \pm 0.2$	$3.4 \pm 1.4$
P4	19 Dec 2014	02:50 – 05:40	1.1	$1.14 \pm 0.06$		
22-23 December 2014						
P1	22 Dec 2014	15:10 – 17:40 <sup>a</sup>	1.9	$1.85 \pm 0.08$		$2.0 \pm 0.8$
P2	22 Dec 2014	18:45 – 21:40 <sup>b</sup>	1.7	$1.68 \pm 0.07$		$1.9 \pm 0.8$
P3	22–23 Dec 2014	23:40 <sup>b</sup> – 01:40	1.4	$1.38 \pm 0.10$		$2.1 \pm 0.9$
P4	23 Dec 2014	02:40 – 05:40	1.1	$1.10 \pm 0.06$		$1.2 \pm 0.5$

<sup>a</sup> The HI Ly $\beta$  brightnesses over P1 on 22 December 2014 are calculated up to 17:25 UT (see Figure 3b), as the differential flux from the electron spectrometer is not reliable for the rest of P1. <sup>b</sup> The HI Ly $\beta$  brightnesses over P2 and P3 on 22 December 2014 are calculated up to 22:00 UT and from 23:10 UT, respectively (see Figure 3b) in order to show the trend driven by the variability in the measured electron differential flux.

**Table 3: Extended Data Table 1. Examples of Rosetta simultaneous measurements.** This dataset has been used for calculating the FUV atomic emission brightnesses at two times during FUV nadir-viewing observation periods (fourth and fifth cases in Figure 2): (1) the electron differential flux  $J_e$  (see Extended Data Fig.1) measured by the RPC–IES electron spectrometer at the selected day and start time  $t^{\text{IES}}$  (first and second columns), at a cometocentric distance  $r_R$  (third column), and associated with a number density  $n_e^{\text{IES}}$  (fourth column) and mean energy  $E_e^{\text{IES}}$  (fifth column) of electrons with energies between 10 eV and 200 eV; (2) the total neutral density  $n_{\text{tot}}^{\text{COPS}}$  measured by the ROSINA–COPS pressure gauge (sixth column) from which the column density  $C^{\text{COPS}}$  is derived (seventh column); (3) the neutral composition measured by the ROSINA–DFMS neutral mass spectrometer and given in terms of volume mixing ratio  $v_n$  of the four major neutral species (eighth column).

Selected day	$t^{\text{IES}}$	$r_R$	$n_e^{\text{IES}}$	$E_e^{\text{IES}}$	$n_{\text{tot}}^{\text{COPS}}$	$C^{\text{COPS}}$	$v_n^{\text{DFMS}}$
	(UT)	(km)	( $\text{cm}^{-3}$ )	(eV)	( $\text{cm}^{-3}$ )	( $10^{15} \text{ cm}^{-2}$ )	H <sub>2</sub> O, CO <sub>2</sub> , CO, O <sub>2</sub> (%)
29 Mar 2015	11:47:18	92	30 <sup>a</sup>	31 <sup>a</sup>	$12.5 \times 10^6$	6.2 <sup>b</sup>	96, 1.4, 1.6, 1.0 <sup>c</sup>
26 Dec 2015	08:35:08	79	1 <sup>a</sup>	20 <sup>a</sup>	$13.5 \times 10^6$	4.9 <sup>b</sup>	95, 2.5, 1.1, 1.4 <sup>c</sup>

<sup>a</sup> The number density  $n_e$  (fourth column) and mean energy (fifth column) of electrons with energies between 10 eV and 200 eV are derived by integrating the differential electron flux  $J_e$  (corrected for the spacecraft potential) over the velocity space. These quantities are given for information; only  $J_e$ , not its moments, is used in the calculation of the modelled FUV brightnesses. <sup>b</sup> The total column density is derived from the total neutral density  $n_{\text{tot}}$  assuming a mean cometocentric distance for the nucleus' surface of 1.7 km<sup>48</sup> (see Eq. 4). <sup>c</sup> The volume mixing ratio for the four major neutral species is obtained from the ROSINA/DFMS mass spectrometer (other species are neglected).



Energetic  
electron

Cometary  
molecule

Excited  
atom

HI and OI auroral  
emissions

RPC

ROSINA  
MIRO, VIRTIS

Alice

Modelled brightness

Observed brightness



